PROCEEDINGS A

royalsocietypublishing.org/journal/rspa

Research



Cite this article: Fullard LA, Breard ECP, Davies CE, Godfrey AJR, Fukuoka M, Wade A, Dufek J, Lube G. 2019 The dynamics of granular flow from a silo with two symmetric openings. *Proc. R. Soc. A* **475**: 20180462.

http://dx.doi.org/10.1098/rspa.2018.0462

Received: 12 July 2018

Accepted: 29 November 2018

Subject Areas:

fluid mechanics, geophysics, mathematical modelling

Keywords:

discrete element modelling, particle image velocimetry, granular flow, silo, granular interference, granular friction

Author for correspondence:

L.A. Fullard

e-mail: l.fullard@massey.ac.nz

Electronic supplementary material is available online at https://dx.doi.org/10.6084/m9. figshare.c.4342265.

The dynamics of granular flow from a silo with two symmetric openings

L. A. Fullard¹, E. C. P. Breard⁴, C. E. Davies², A. J. R. Godfrey¹, M. Fukuoka², A. Wade², J. Dufek⁴ and G. Lube³

¹Institute of Fundamental Sciences, ²School of Engineering and Advanced Technology, and ³Volcanic Risk Solutions, Massey University, Palmerston North, New Zealand ⁴Department of Earth Sciences, University of Oregon, Eugene, OR, USA

LAF, 0000-0002-9193-8664

The dynamics of granular flow in a rectangular silo with two symmetrically placed exit openings is investigated using particle image velocimetry (PIV), flow rate measurements and discrete element modelling (DEM). The flow of mustard seeds in a Perspex silo is recorded using a high-speed camera and the resulting image frames are analysed using PIV to obtain velocity, velocity divergence and shear rate plots. A change in flow structure is observed as the distance L between the two openings is varied. The mass flow rate is shown to be at a maximum at zero opening separation, decreasing as L is increased; it then reaches a minimum before rising to an equilibrium rate close to two times that of an isolated (non-interacting) opening. The flow rate experiment is repeated using amaranth and screened sand and similar behaviour is observed. Although this result is in contrast with some recent DEM and physical experiments in silo systems, this effect has been reported in an analogous system: the evacuation of pedestrians from a room through two doors. Our experimental results are replicated using DEM and we show that inter-particle friction controls the flow rate behaviour and explains the discrepancies in the literature results.

1. Introduction

The gravity-driven flow of granular material has fascinated mankind for millennia, whether from hour-glass devices to track time or silos to store grain and other granular produce [1,2]. In the present time, industrial processing of granular materials is common and silos are regularly used as storage vessels. The physics of granular flow in general is under-developed when compared with that of traditional Newtonian fluids such as water [3], mostly because of the different states (solid-like, liquid-like, gas-like) in which the granular material can exist [4].

While there has been much progress in classifying granular behaviour experimentally [5–11] and using mathematical modelling [12-15], there remains a need for further work to fully understand the physics of granular phenomena. For silo flows, in particular, there is a large body of experimental and numerical work ([16-25], for example). Most silo studies focus on the case where there is a single silo opening (where the particles discharge under gravity) located at the centre of the silo. However, there has been increasing interest in variants of this standard case including eccentric positioning of a single opening [26,27], a vertically oriented opening [28], submerged silo flows [29,30] and in silos with particles of non-spherical shape [31,32]. One variant, in particular, is where there exists more than one opening at the bottom of the silo. In recent times, this multi-opening case has been examined and it was found that the positioning of two openings can significantly change jamming dynamics in a silo. In particular, it was found in discrete element modelling (DEM) simulations that the presence of a second nearby opening allowed spontaneous jamming and unjamming of an orifice, and the probability of jamming decreased as the openings were moved closer together [33,34]. Furthermore, DEM experiments were carried out to show how mixing could be controlled in a silo with multiple openings. It was shown that stagnant zones could be reduced and a more uniform particle distribution across the silo could be obtained when opening and closing adjacent openings at an appropriate frequency [35]. In recent experimental work [36], the velocity of particle flow in silos with two openings was mapped using particle image velocimetry (PIV) for two symmetrically and then eccentrically placed openings. The mass flow in the double symmetric case was found to be (almost) two times the flow rate through a single opening. It was also noted that the mass flow rate increases when the openings were adjoining the silo wall. The authors additionally modified the well-known Hagen-Beverloo flow rate to account for two symmetrically and eccentrically placed openings. However, the authors caution that the model will not apply when the openings are close together owing to interaction of the flow zones. The mass flow rate of a silo with two adjacent openings (placed symmetrically) in a silo was investigated using DEM [37] and it was found that the maximum flow rate occurred when the openings converged into a single larger opening, with the flow rate then monotonically decreasing exponentially to a steady state as the openings were separated. Again, it was noted that the flow rate for two non-interacting openings (i.e. placed far apart) was equal to two times the flow rate of a single opening. Xu et al. [38] performed silo drainage experiments with steel spheres and also found similar monotonic decreasing flow rate behaviour. However, their silo was only quasi-three dimensional (the depth was of the order of a single particle diameter), they had only one opening separation distance L smaller than the particle diameter and steel has a relatively small friction coefficient compared with many other granular materials such as grains, seeds or sand. Davies et al. [39] previously performed experiments to quantify the flow rate from a multi-opening cylindrical drum, and also studied the effect of changing the spacing between openings. They found that hexagonally arranged openings reduced the flow rate more than other arrangements. However, work using a social force model on an analogous system, the evacuation of pedestrians from a room with two exit doors [40], has shown a different dynamic as two exit doors were separated. Using this model it was shown that the time to exit the room was quickest when two doors of equal size were merged into one large door (largest flow rate, similar to the DEM result); however, as the doors were separated, the time to evacuate the room increased (decreasing flow rate), reached a maximum (minimum flow rate) and then decreased (increasing flow rate) to a steady time slightly less than half the time of a single exit door. This flow rate minimum was said to occur as a result of the increased 'pressure'

effects acting on pedestrians. It is unclear if this dynamic is unique to the pedestrian system, or if it can occur in gravity-driven granular particle flows also. We note that the flow of pedestrians through doors has previously been experimentally studied as an analogue to jamming of granular materials in a silo [41].

The purpose of the current work is to investigate the kinematics of silos with two symmetrically placed openings through mass flow rate and PIV measurements. We aim to generate the experimental data to determine what type of flow rate behaviour occurs in the case of two symmetric openings: the monotonic decreasing flow rate behaviour found using DEM [37] or the local minimum rising to a steady rate found in the pedestrian system [40]. This is achieved by experimentally measuring the mass flow rate from the silo as a function of opening spacing (including for spacings less than the particle diameter) for different opening sizes and a range of granular materials. We then use PIV to generate velocity maps over a wide range of opening separations (in contrast to earlier work where the case of closely spaced openings was not investigated [36]). Finally, we use DEM to investigate the system and obtain parameters not available from the physical experiment which help us to explain the observed phenomena.

2. Methods

The experimental system is displayed in figure 1. The test area consists of a rectangular silo of width W = 200 mm, height H = 350 mm and depth D = 15 mm. In previous experiments in silos with two openings, the silo depth has allowed a single layer of flowing particles only [38]. In this work, the silo depth was chosen to be at least six times larger than the particle diameter to produce a more realistic flow condition, while still ensuring that the flow was primarily two dimensional (2D). Above the test area is a feed hopper which keeps the test area filled with particles. At the bottom of the test area are two interchangeable exit openings, each of size D_0 , separated by a distance L. Note that we may set L = 0, which corresponds to a single orifice of width $2D_0$, or we may use a single orifice of size D_0 . The openings are symmetrically located around the silo axis. Below the silo there is a collector bucket that sits atop a load cell, which enables us to dynamically measure the mass of particles and, hence, determine the mass flow rate of the system.

The silo test area was loaded from above using a rain-filling method to ensure consistent packing. For the PIV experiments, mustard seeds were selected with a Sauter mean particle diameter (SMD) of 2.15 mm, while for the mass flow experiments amaranth seeds (SMD of 1.08 mm) and sand (screened to a size range between 0.355 and 0.6 mm with SMD of 0.46 mm) were used in addition to the mustard seeds. To avoid jamming the individual opening width, D_0 was selected to be greater than six times the particle diameter, d. The mass flow experiments with amaranth were repeated with two opening widths ($D_0 \approx 7.5 \times d$ and $D_0 \approx 13 \times d$) to ensure that the results were independent of the ratio of D_0 to d. The PIV and mass flow experiments were conducted firstly with a single opening of size D_0 , then a single opening of size D_0 , and then for two symmetrically placed openings with spacing L=0.5, 0.75, 1, 1.25, 1.5, 2, 4, 8, 16, 32, 48 and 80 mm. The openings were laser cut to ensure accuracy in their dimensions. The SMD, d, and opening widths, D_0 , for each experiment are listed in table 1.

To obtain the velocity maps during the PIV experiments on the mustard seeds, the silo was illuminated with ultra-bright LED light and the flow was recorded using a camera (Basler acA2000-340 km) that had high definition, high speed and recorded 500 frames per second (FPS) in black and white. Each frame was then downsampled to 62.5 FPS and processed using the software PIVlab [42,43]. To reduce PIV noise error, once a steady flow was established 5 s of images were analysed and then averaged to achieve a smooth velocity field. Silos have been shown to have an initial transient in the development of the steady velocity field (but not in the flow rate) [18], so the 5 s of images was selected after approximately 40 s of flow to ensure that the steady regime had been reached. This averaged 2D velocity field could then be used to calculate its divergence and the shear rate of the flow as detailed in §4.

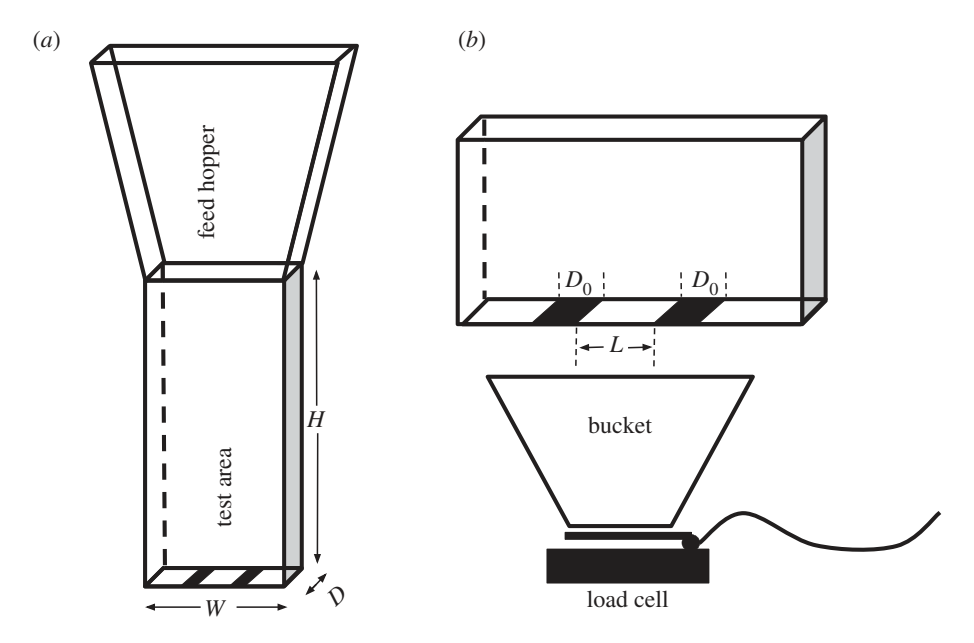


Figure 1. (a) The Perspex silo experimental apparatus used for this study. (b) A close-up of the two symmetric openings and the mass flow rate measuring system.

Table 1. Particle diameter, d, and opening width, D_0 , for each experiment.

	PIV exp.	mass flow exp.	<i>d</i> (mm)	D_0 (mm)
mustard seed	✓	✓	2.15	14
amaranth seed		✓	1.08	8 and 14
screened sand		✓	0.46	8

The mass flow rate for each experiment (varying L, D_0 and particle type) was measured using a bucket atop a load cell. The total mass as a function of time was logged in real time at 100 Hz; the slope of this total mass versus time plot gave the mass flow rate.

3. Mass flow rate results

In order to understand the effect of the spacing L between the two openings on the mass flow rate, and to provide experimental data on double opening flow interaction, we conducted flow rate experiments with three granular materials: mustard seeds (SMD 2.15 mm), amaranth seeds (SMD 1.08 mm) and sand (SMD 0.46 mm). The size of each opening, D_0 , for each experiment is given in table 1. Note that we performed the amaranth experiment twice, the second time with a larger D_0 (as noted in the table), in order to test if there is an effect of the ratio of opening size to particle size (D_0/d) . The total mass of discharge was dynamically recorded with a bucket placed on a load cell system. The current mass was recorded to a PC at 100 Hz and stored as a spreadsheet file. To obtain the mass flow a linear least squares fit was performed on the mass versus time data. For reference, the mass flow rate, Q, of particles of diameter d from a rectangular silo with a single opening of size D_0 is given by the Hagen–Beverloo relationship [44],

$$Q = C\rho \sqrt{g}(D_0 - kd)^{3/2}, \tag{3.1}$$

where ρ is the bulk density, g is gravity and C, k are constants.

Figure 2 displays the results of the experimental series. The flow rate for each set of experiments has been normalized by the flow rate from a single opening of size $2 \times D_0$ (since

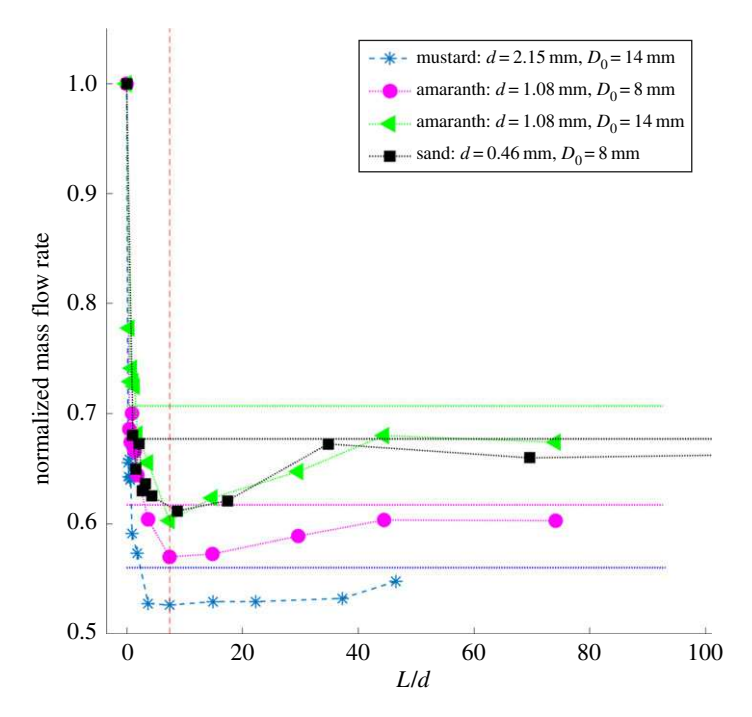


Figure 2. The mass flow rate normalized by the rate from a single large opening as a function of spacing/particle diameter L/d for the different experiments. Error bars are smaller than the symbol size. (Online version in colour.)

this opening produces the largest flow rate). The normalized flow rate has been plotted versus L/d, with d the particle diameter. The horizontal lines indicate two times the flow rate through a single opening of size D_0 . It is apparent in each of the experiments that we do not have monotonic behaviour (as seen using DEM in previous modelling work [37]), but in fact we have a local minimum at a critical value of spacing L/d. This same flow rate interference pattern was noted in the evacuation of pedestrians from a door with two exits [40]. The minimum flow rate for the mustard seed case occurred at $L/d \approx 7.5$, which is approximately when the two openings separated from each other's influence (see §4). For the other particles tested, the mass flow rate minimum also occurs at approximately the same location ($L/d \approx 7.5$, denoted in figure 2 by the red dashed vertical line). This is larger than for the pedestrian exiting a room case [40], where the minimum flow rate occurred at $L/d \approx 4$, but it should be noted that the exit opening compared with pedestrian size was only fourfold, hence that work was in the jamming regime, whereas here our openings are wide enough to ensure free flow.

With the exception of the sand, as L/d increases the flow rates approach, but do not reach, the previously predicted two times the flow rate of a single opening of width D_0 (denoted by the dotted horizontal lines in figure 2). This is possibly due to the finite silo width; in an infinitely wide silo with L very large we would expect to fully recover the two times single opening flow rate. We note that this limiting flow rate is different for different grains, grain diameters and different ratios of the opening width to particle diameter. This effect is fully accounted for by the kd term in the Hagen–Beverloo equation (3.1). Considering the two amaranth experiments, the pattern of flow is identical (with the exception of the higher flow rate for the $D_0 = 14 \, \mathrm{mm}$ case, accounted for by the kd term in equation (3.1)). Therefore, we conclude that the ratio of opening width to particle diameter does not alter the qualitative behaviour, apart from the expected flow rate effect. For each of figures 2 and 3 the error bars are less than the size of the plot markers.

Figure 3 is a zoomed-in version of the mass flow rate results of figure 2. In this figure, we see the flow rate behaviour when the two orifices are very close together and interacting strongly. It

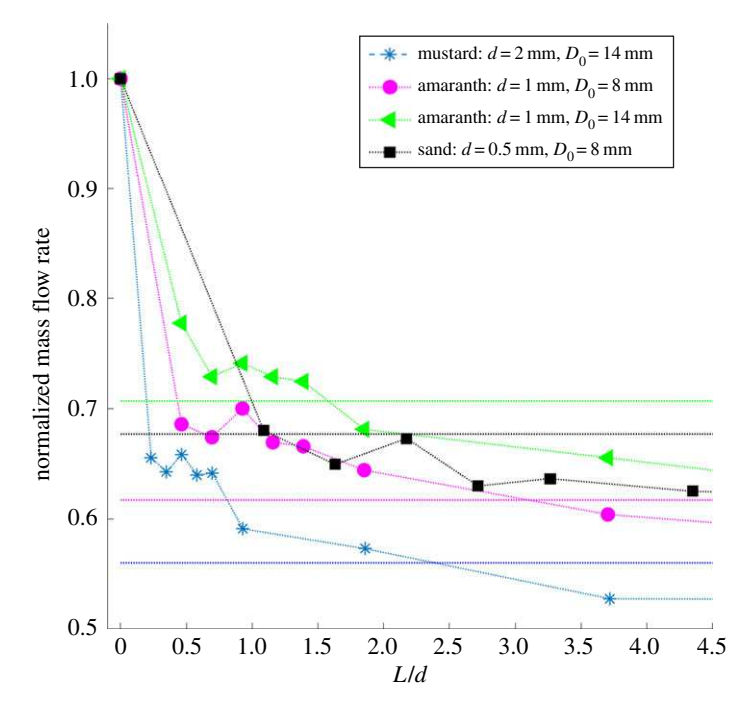


Figure 3. A zoomed-in version of figure 2. Error bars are smaller than the symbol size. (Online version in colour.)

is apparent that in each experiment, below around L/d=4, there is an instability in the flow rate as L is modified. We have independently verified this observation by estimating the volumetric flow rate per unit depth of the silo. We took the PIV images and integrated the vertical component across the width of the silo to obtain the volumetric flow rate per unit depth. The same instability was observed in those data. The observed instability for two openings very close together has not been previously reported. We hypothesize that this occurs when the interaction between two openings is very strong and consequently particles feel strong attraction to both openings, leading to increased 'competition' between particles to exit the silo. Therefore, this could be related to a 'faster-is-slower' effect [45]. Further work is needed to identify the origin of the instability for small values of L. Similar fluctuations in the flow rate from silos has previously been observed in narrow silos with a single opening [46], which was reportedly due to clogging and unclogging dynamics in the silo. Here, our result is related to the interaction between two nearby openings.

4. Particle imaging velocimetry results

For the PIV experiments, the discharge of mustard seeds was recorded, varying the spacing, L, between the two openings. The resulting image frames were processed using PIVLab and the velocity vectors, \mathbf{u} , at steady state derived and displayed in §4a. Using the resulting 2D velocity fields the divergence of velocity ($\nabla \cdot \mathbf{u}$; §4b), and the 2D tensorial shear rate ($\dot{\gamma} = \sqrt{(\partial_x u_y + \partial_y u_x)^2 + (\partial_x u_x - \partial_y u_y)^2}$, where u_x , u_y are the horizontal and vertical velocity components derived from the PIV analysis; §4c) were calculated.

(a) Velocity field

The averaged steady velocity fields, calculated from PIV analysis, are shown in figure 4 for the flow of mustard seed through two single opening cases (figure 4a) and for the 12 cases where there are two openings separated by a distance L (figure 4b). The figure plots the magnitude of the velocity vector at each location. It is evident from the plots with two openings that for $L \lesssim$

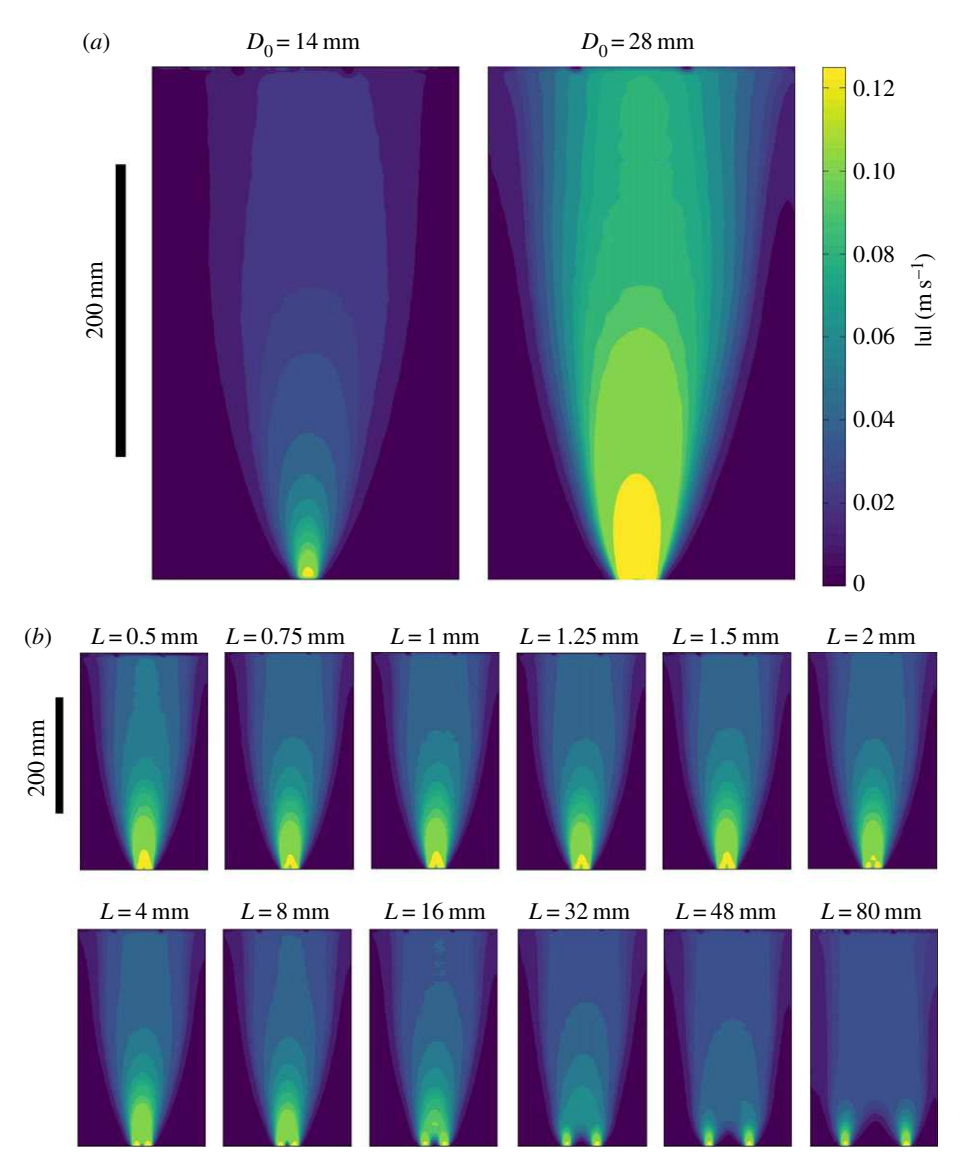


Figure 4. The magnitude of the mean velocity vector for the flow of mustard seeds through the silo. (*a*) Single openings; (*b*) two openings spaced by a distance *L*. There is a small amount of noise introduced to the velocity field by the PIV algorithm; however, this is small and does not significantly alter the qualitative and quantitative features of the analysis. (Online version in colour.)

2 mm the qualitative behaviour close to the orifice is similar. The two openings behave as a single opening with velocity magnitude between the two single opening cases. At around L=2 mm, the gap between the two openings becomes more apparent and a zone of positive interference appears midway between the two openings. By L=16 mm the zone of interaction midway above the openings begins to break down until the two openings appear to cease to interact from $L \gtrsim 32$ mm. At the larger values of L, when the two openings cease to interact, the individual velocity profiles close to each opening appear to be of similar magnitude to the small single opening case ($D_0=14$ mm). To further illustrate this interaction behaviour we plot the downwards flow velocity along a horizontal slice close to the openings. Figure 5 displays the downwards velocity at a distance of 25 mm above the openings. In figure 5a, for $L \leq 2$ mm, it is apparent that a single peak

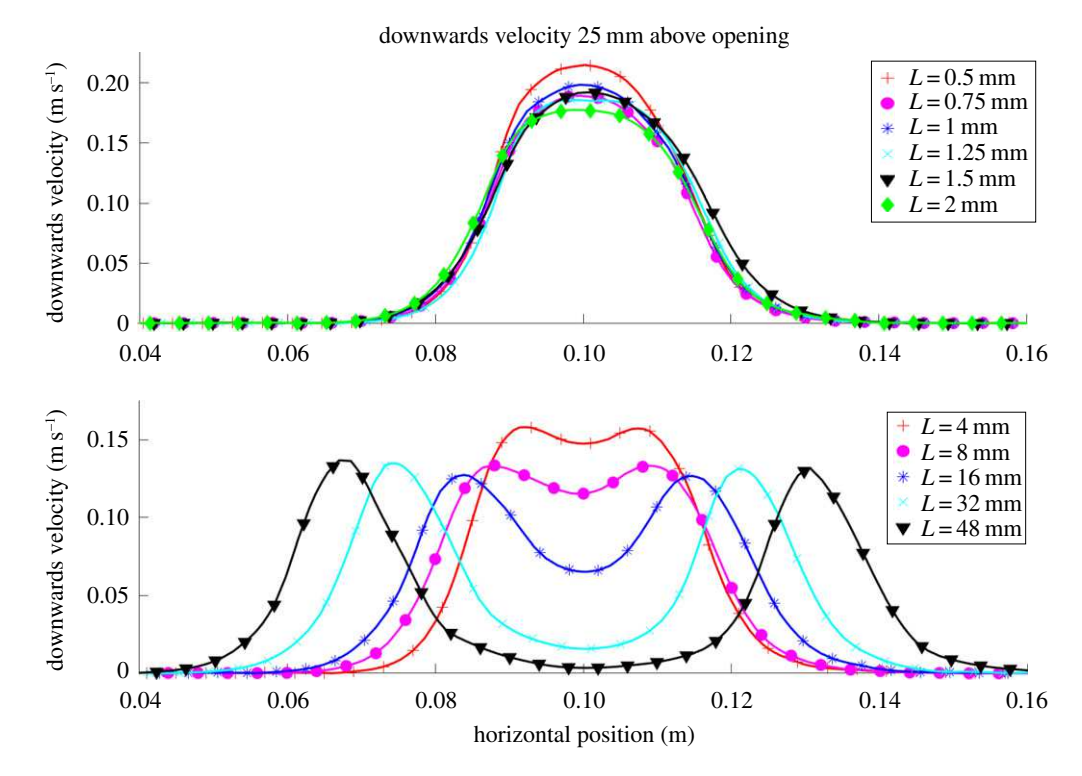


Figure 5. Downwards velocity profiles along a horizontal slice 25 mm above the silo openings. Error bars (due to PIV algorithm noise) are of the order of the symbol size. (Online version in colour.)

is formed and the two openings are behaving as a single one. In figure 5b, $L \ge 4$ mm, two peaks are formed and the flow interaction between the two openings becomes weaker as the spacing between the openings is increased. By ≈ 48 mm the openings seem to be interacting very weakly or not at all. For large L, far from the orifice, the velocity in the bulk of the silo appears to be fairly uniform, in contrast with the single opening case. Additionally, a heap of material in between the two openings is formed, growing larger as L is increased. In summary, it is shown that for small L (≈ 2 mm or less) the two openings seem to act as a single opening, for large openings (larger than ≈ 32 mm) the two openings have little to no interaction, while there is a complicated interference behaviour in between.

(b) Velocity divergence

Using the velocity fields calculated using PIV analysis, we numerically calculated the divergence of the velocity vector, $\nabla \cdot \mathbf{u}$, for each mustard seed experiment. The zones of light yellow in figure 6 represent areas of the silo flow where the bed is expanding; likewise areas of dark purple indicate bed contraction. Similar to the velocity fields, for $L \lesssim 2$ mm the plots are qualitatively similar to the single opening cases. For values of L larger than 16 mm, there is a zone of negative divergence (compression) which sits on top of the heap which is formed in between the openings. This zone represents areas where the particles must slow, come to a stop, and either flow along the heap or become a part of it. For the largest opening separations, the divergence locally near the openings is individually similar to the small single opening case. We note that the divergence is relatively small in the bulk of the silo, but large near the orifice. This suggests that continuum mathematical models of dense granular silo flow should be compressible multi-phase models so that behaviour near the opening(s) is accurately characterized. We note that the small value of the divergence in the bulk of the silo (i.e. far from the opening) is of the same order of magnitude as the divergence

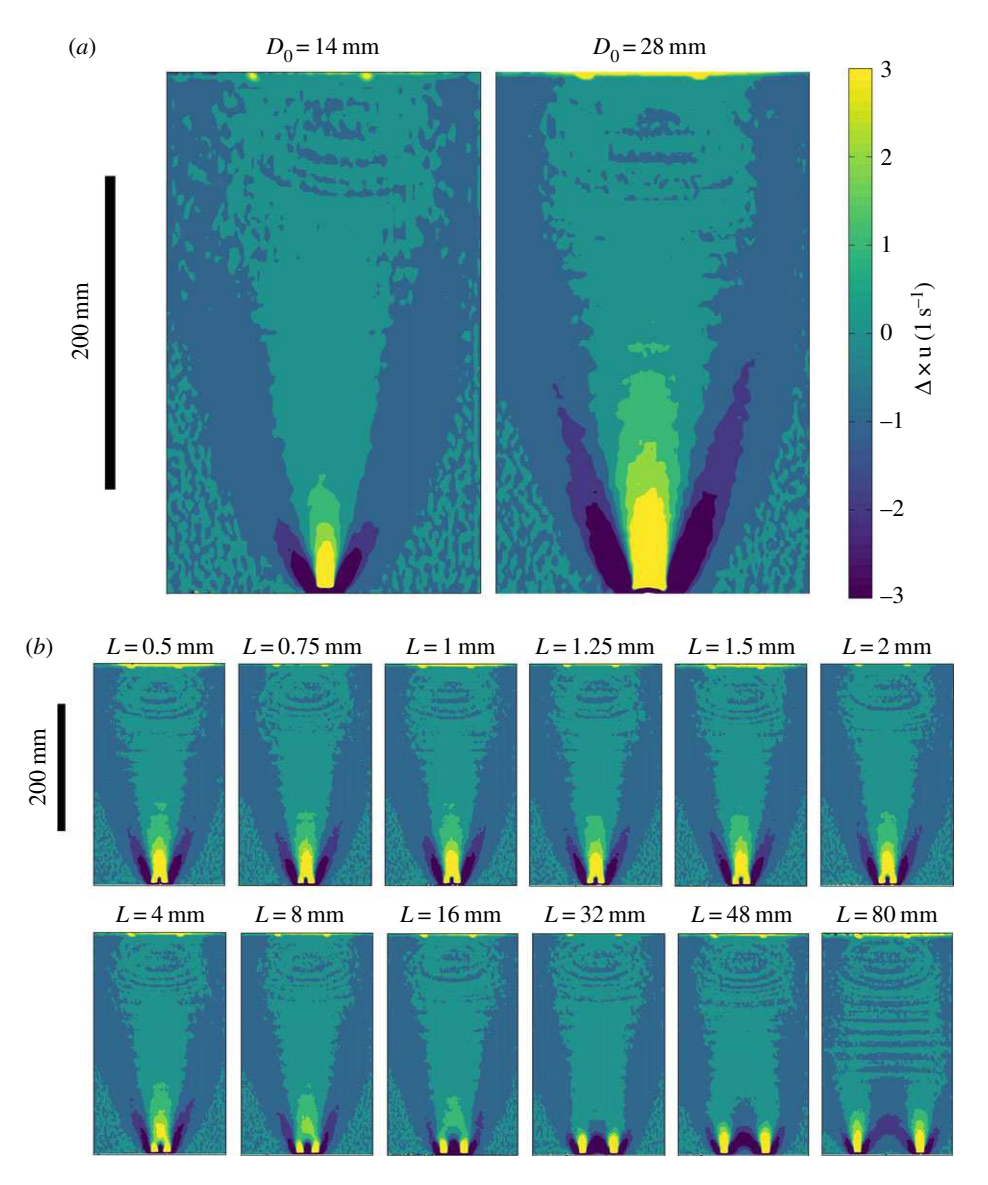


Figure 6. The velocity divergence for the flow of mustard seed through the silo. (*a*) Single openings; (*b*) two openings spaced by a distance *L*. (Online version in colour.)

near the bottom left and right silo regions. By visual inspection, these lower left and right regions were composed of stagnant material. However, the PIV analysis method gives small but non-zero values of velocity in these regions owing to noise; hence, when spatial derivatives of velocity are taken in these stagnant zones, the divergence is also non-zero. Again, by inspection these regions were not dilating; hence, the magnitude of divergence calculated in these regions acts as a bound on the resolution of our divergence measurements. We, therefore, conclude that, in the bulk of the silo regions, far from the silo opening the divergence is too small to be able to state whether particles in this region are dilating or not. A further observation is related to the relative size of the zone of large dilation immediately above each orifice. For $L \lesssim 2 \,\mathrm{mm}$ this zone is roughly a constant size (i.e. the size of the 'light yellow' zone), but this zone rapidly shrinks hereafter, reaching a minimum at $L=8 \,\mathrm{mm}$. As L increases past 8 mm the high dilation zone immediately above each orifice again begins to grow in size and is large again once $L=80 \,\mathrm{mm}$. This result

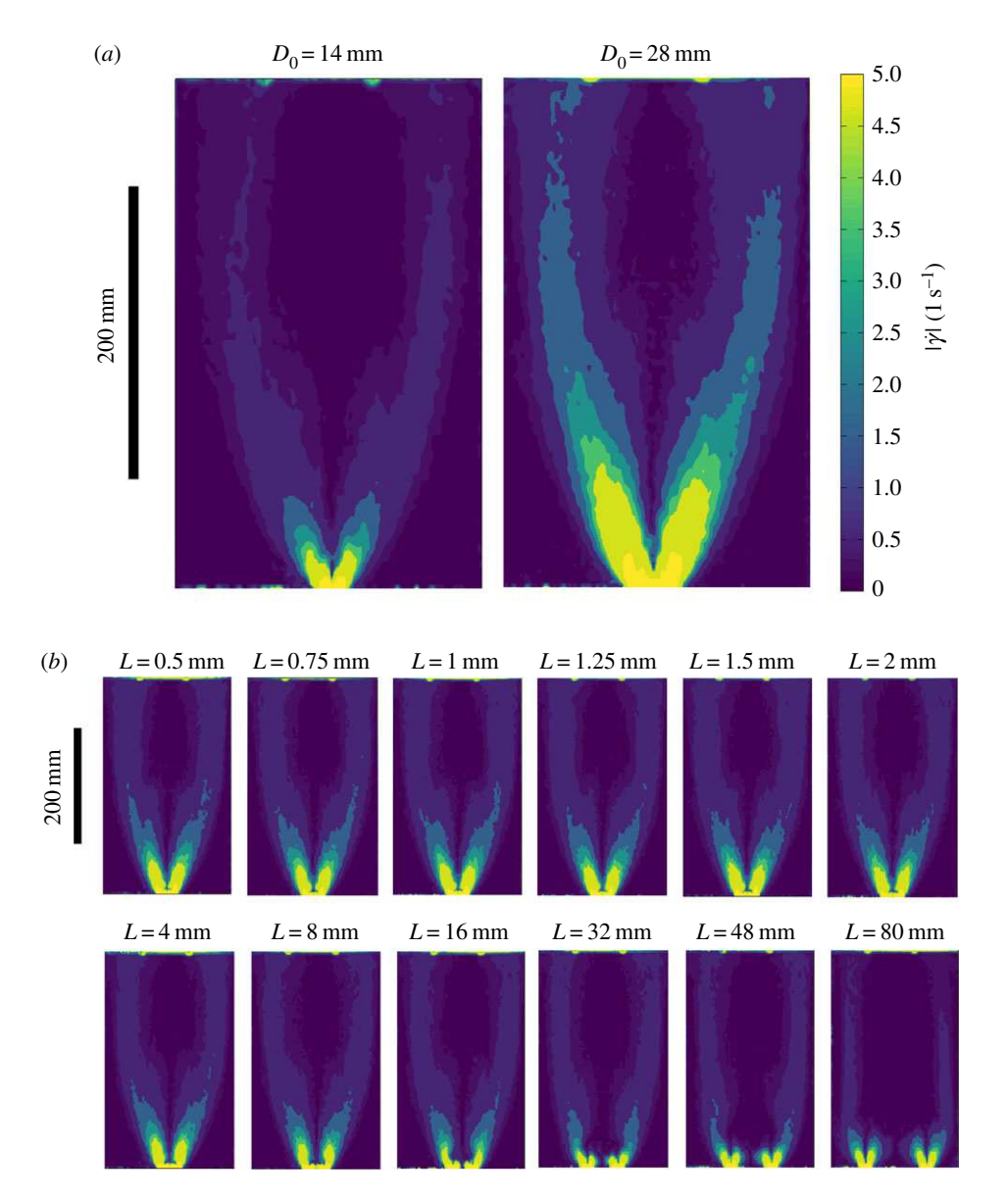


Figure 7. The shear rate magnitude for the flow of mustard seed through the silo. (*a*) Single openings; (*b*) two openings spaced by a distance *L*. (Online version in colour.)

appears to suggest that the bulk density at the openings has a maximum at a critical separation, *L*, and has the potential to cause a 'faster-is-slower' effect [45].

(c) Shear rate

To locate regions of high and low/no shear, and to investigate the effect of L on these regions, we calculate the 2D tensorial shear rate for each experiment, $\dot{\gamma} = \sqrt{(\partial_x u_y + \partial_y u_x)^2 + (\partial_x u_x - \partial_y u_y)^2}$. The results are shown in figure 7. A similar pattern to the previous two figures is noted; the plots are qualitatively very similar for L < 2 mm, an apparent interaction zone for L > 2 mm but less than $L \approx 16$ mm, and then no apparent interaction for larger L. The largest shear rates occur near the opening, as expected, but there are two shear bands that appear as 'arms' left and right of the

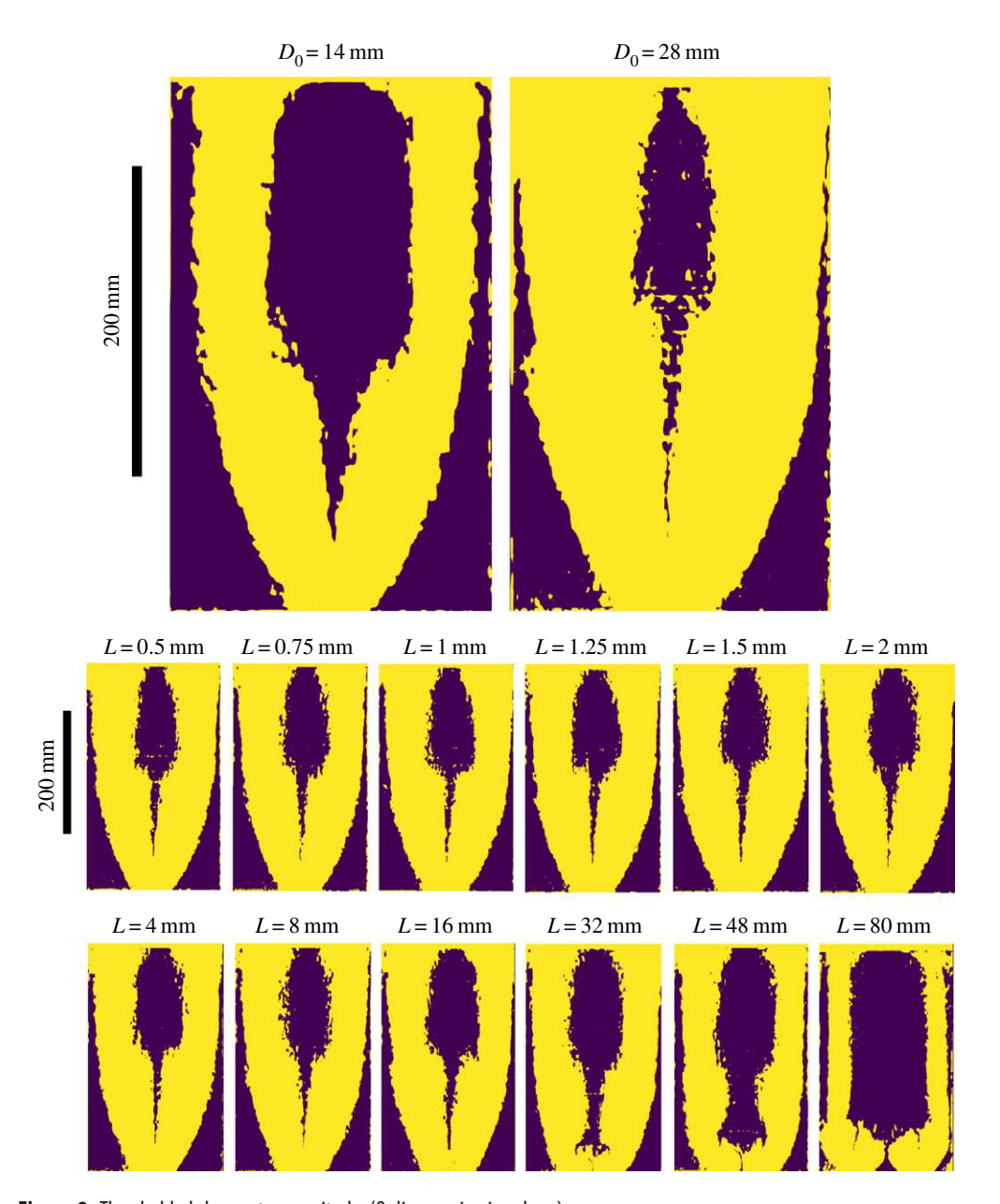


Figure 8. Thresholded shear rate magnitude. (Online version in colour.)

silo centre, then extend to the top of the silo. In between these arms is a region of very low shear which appears to expand in area as L increases (for $L \gtrsim 2\,\mathrm{mm}$). To further visualize this effect, we apply a threshold to the shear rate magnitude for each experiment. Even in stagnant areas the PIV analysis will produce small velocities, since it is a noisy algorithm, yet there are regions in the flow which we know from inspection are stagnant (for example, material near the bottom left and right corners for single openings, or in the 'heap' between two widely spaced openings). Therefore, for each experiment, we analyse the mean and standard deviation of the shear rate magnitude in these regions, which are known to be stagnant. The threshold value is then defined to be the mean +3 standard deviations and was applied to the entire silo area. This thresholded version of the shear rate magnitude plot is displayed in figure 8, with light yellow regions where

the threshold is exceeded and dark purple regions where the shear rate magnitude is lower than the threshold.

Clearly, the low shear rate region grows for large values of *L*, approaches closer to the openings, and the shear band zones on either side shrink. This observation could have important implications for mixing of polydisperse granular materials, since it is known that the rate of flow-induced segregation is proportional to the shear rate. Further work is required to conclude what effect multiple openings (and their spacing) has on mixing and segregation of granular materials.

5. Discrete element modelling

We attempt to gain insights into the observed phenomena of the previous sections using modelling techniques. DEM numerical simulations were performed using the Multiphase Flow with Interface eXchange (MFIX) numerical open-source code which is developed and supported by the US Department of Energy and National Energy Technology Laboratory (the code used to produce the DEM simulations is freely available at https://mfix.netl.doe.gov/). We adopted this approach to simulate particle–particle interactions [47]. Collisions and frictional contacts between particles were modelled using a soft-sphere approach, which uses a spring-dashpot model [47]. The granular material is modelled as N_m Lagrangian spheres of diameter D_m and solid particle density ρ_p . Each particle's momentum and position is quantified by solving Newton's laws of motion,

$$\frac{dX^{(i)}(t)}{dt} = V^{(i)}(t),\tag{5.1}$$

$$m^{(i)} \frac{\mathrm{d}V^{(i)}(t)}{\mathrm{d}t} = F_T^{(i)}(t) = m^{(i)}\mathbf{g} + F_d^{(i \in k, m)}(t) + F_c^{(i)}(t), \tag{5.2}$$

$$I^{(i)}\frac{d\omega^{(i)}(t)}{dt} = T^{(i)}(t), \tag{5.3}$$

where $X^{(i)}(t)$ is the particle position of the i-th particle within the domain at time t, $V^{(i)}(t)$ is the particle linear velocity, and $m^{(i)}$ is the particle mass; $F_T^{(i)}$ is the sum of all forces acting on the i-th particle, $F_d^{(i \in k, m)}$ is the total (viscous and pressure) drag force acting on particle 'i' if the m-th solid phase is located within the k-th cell, $\omega^{(i)}$ is the angular velocity of the i-th particle, $F_c^{(i)}$ is the net contact force resulting from contacts with other particles; $T^{(i)}$ is the sum of all torques acting on the i-th particle, and $I^{(i)}$ is the moment of inertia.

Since particle interactions are explicitly modelled in the DEM approach we can extract fine detail about the local state of the flowing granular system that would not be possible using a continuum model. The soft-sphere DEM model is a robust method to simulate granular dynamics, in part because of the independence of the time-step size on the particle volumetric concentration [47,48].

In this soft-sphere approach, the overlap between particles is represented by a series of springs and dashpots in the normal and tangential directions. The dashpot is used to model the loss of kinetic energy during inelastic collisions, while the spring models the rebound of a particle which is in contact with another. Both dashpot and spring are described with dampening and stiffness coefficients in both the tangential and normal directions. The spring–dashpot model of MFIX has been rigorously validated in a series of studies [47,48]. For more information regarding the physics of the spring–dashpot model, please refer to Garg *et al.* [47].

We seek to reproduce our physical experiments with the MFIX DEM models to try to explain the behaviour observed. Furthermore, we examine the effect of having a low and high value of particle–particle friction on the dynamics of the flow as the spacing, L, between openings is varied. In total 134 166 particles were modelled, to which we attributed a density of 1202 kg m $^{-3}$ (this is equal to the density of mustard seeds, which was measured with a nitrogen pycnometer). Frictional properties of the particle–particle and particle–wall interactions were chosen to match literature and experimental values. The static friction coefficient of the particles was 0.2 for the

low-friction case (as in Zhang $et\ al.$ [37]) and 0.53 for the high-friction simulations (obtained by measuring the angle of repose of the mustard seeds). The particle–wall friction coefficient used was 0.2 for the low-friction DEM simulations (as in Zhang $et\ al.$ [37]) and 0.4 in the high-friction case. The restitution coefficient of 0.6 was obtained from the literature values [49]. The value used for the particle stiffness coefficients (k_n and k_t) was 10^4 , which is well above the minimum value needed for particle contacts to be within the hard regime. Note that no fluid interaction was present in the simulation.

The silo dimensions in the DEM simulations are exactly those of the physical experiment. The opening dimensions used were $0.015\,\mathrm{m}$ in depth and $0.014\,\mathrm{m}$ in width. The spacings between openings, L, were: 0.5, 0.75, 1, 1.25, 1.5, 2, 4, 8, 16, 32, 48, $80\,\mathrm{mm}$, as in the physical experiment. Additionally, we also model the single opening cases, with opening widths of 14 and $28\,\mathrm{mm}$. The $28\,\mathrm{mm}$ single opening case is equivalent to the case with two openings, separated by a distance $L=0\,\mathrm{mm}$.

(a) Discrete element method results

(i) Flow rate

By counting the number of particles exiting the silo in a 200 ms time period we obtain a measure of the flow rate. By inspection, this flow rate was constant over time (assuming the silo was filled enough). As in the experimental case, the error bars are less than the size of the plot markers. The flow rates as a function of the opening spacing, L, for both the low- and high-friction cases (normalized by the flow through a single opening of width 28 mm) are shown in figure 9. It is immediately clear that there is a difference in behaviour between the low- and high-friction cases. In the low-friction case, the normalized flow rate appears to be monotonically decreasing as L is increased (as observed in previous silo studies [37,38]). However, in the high-friction case there is a clear minimum in the flow rate at $L/d \approx 8$ mm (approx. the same location as in our physical experiments; figure 2), with the flow rate rising to the equilibrium rate as L is increased further (as observed in our physical experiment, and in pedestrian dynamics models [40]). Recall that in the high-friction simulation the inter-grain friction coefficient matches the coefficient of the real grains. The observation that the qualitative flow rate behaviour is similar between the PIV and high-friction DEM experiments gives us confidence that the DEM model is capturing the dynamics of the real system. It is, therefore, apparent that the two behaviours observed in the literature as L is increased, monotonic decreasing and flow rate minimum, are dependent on the friction between particles and their container. Furthermore, as observed in our physical experiment, the flow rate rapidly decreases from its maximum (single 28 mm opening) as L becomes greater than zero, and for $L < 2 \,\mathrm{mm}$ the flow rate oscillates around a roughly consistent value (as noted in figure 9b). Although the rapid jump in flow rate as L increases from 0 has previously been observed in the literature [38], the oscillatory behaviour has not previously been observed or discussed, yet here it has been found in both physical and DEM experiments. A short video of a selected DEM experiment can be found in the electronic supplementary material.

(ii) Coarse graining near the silo opening

To understand the origin of the observed behaviour, we seek to study continuum fields in the silo near the opening where particles exit the silo. In order to generate continuum fields (velocity, pressure, solids fraction) we apply coarse graining to our DEM results. Given the individual particle positions, velocities and interaction forces, we can generate coarse-grained macroscopic continuum fields to be used to further study the silo system [22,50]. Given N_m number of particles in a simulation, the macroscopic density field can be defined at a point in space, \mathbf{r} , at time t,

$$\rho^{CG} = \sum_{i=1}^{N_m} m_i W \left(\mathbf{r} - \mathbf{r}_i(t) \right), \tag{5.4}$$

Figure 9. Normalized flow rate as a function of opening spacing *L* for the DEM numerical experiments. (*b*) The graph is zoomed to see the effect of small opening separations. Error bars are smaller than the symbol size. (Online version in colour.)

where m_i is the mass of particle i and $\mathbf{r}_i(t)$ is the centre of particle i. The function $W(\mathbf{r})$ is called the coarse-graining function and acts to weight the influence of particles so that those closest to the point of interest, \mathbf{r} , are highly weighted, while those far away are neglected in the sum. Its mathematical definition is given as

$$W(\mathbf{r}) = \begin{cases} V_w^{-1} \exp \frac{-|\mathbf{r}|^2}{2w^2}, & \text{for } |\mathbf{r}| < c \\ 0, & \text{otherwise} \end{cases},$$
(5.5)

where c=3w is the cut-off length, w is the coarse-graining width, taken as one particle diameter (w=d), and V_w is a constant chosen to ensure that the integral of the density is equal to the total mass. Here, we use $V_w=2\sqrt{2}\pi^{3/2}w^3\text{erf}^3(\sqrt{2}c/2w)$.

Similarly, the coarse-grained momentum density (vector), \mathbf{p}^{CG} , is given as

$$\mathbf{p}^{CG} = \sum_{i=1}^{N_m} m_i \mathbf{v}_i W \left(\mathbf{r} - \mathbf{r}_i(t) \right), \tag{5.6}$$

where \mathbf{v}_i is the velocity vector of particle i. The coarse-grained velocity field can then be recovered as $\mathbf{V} = \mathbf{p}^{CG}/\rho^{CG}$.

The stress tensor can be decomposed into kinetic, σ_k , and contact, σ_c , components so that $\sigma = \sigma_k + \sigma_c$. The kinetic component of stress is given as

$$\sigma_k = \sum_{i=1}^{N_m} m_i \mathbf{V}_i' \mathbf{V}_i' \mathbf{W} \left(\mathbf{r} - \mathbf{r}_i(t) \right), \tag{5.7}$$

where V'_i is the fluctuation velocity; $V'_i = v_i(t) - V(r, t)$. The contact stress concerns interactions between two particles in contact, i and j, and is given as

$$\sigma_c = \sum_{i=1}^{N_m} \sum_{j=1}^{N_m} \mathbf{f}_{ij} \mathbf{a}_{ij} \int_0^1 W\left(\mathbf{r} - \mathbf{r}_i(t) + s \mathbf{a}_{ij}\right) \, \mathrm{d}s, \tag{5.8}$$

with $j \neq i$, $\mathbf{f}_{ij} = -\mathbf{f}_{ji}$ are the interaction forces between particles i and j, and $\mathbf{a}_{ij} = \mathbf{r}_i - \mathbf{c}_{ij}$, which is named the branch vector, with \mathbf{c}_{ij} the point of contact between particles i and j.

Defining the macroscopic coarse-grained parameters in the above way ensures that the resulting continuum fields satisfy continuity and momentum conservation [22,50]. To decrease spatial and temporal fluctuations in our coarse-grained fields, we average these fields over the depth of the silo (giving 2D vector fields) and then temporally over a set of 20 time steps (each time step individually is 5 ms). Figures of coarse-grained parameters near the opening of the silo can be found in the electronic supplementary material.

The coarse-graining analysis was performed in a series of steps and substeps to generate figures 10–12, and also the figures in the electronic supplementary material data. These steps are outlined as follows.

- (i) Using equations (5.4)–(5.8), the coarse-graining algorithm was applied to 20 time steps individually. With W the width of the silo and D the depth, for each time step the coarse-graining algorithm was applied to the region $R_1 = W \times D \times (0:5 \text{ cm})$, i.e. over the entire width and depth of the silo, and in the zone from the silo opening to 5 cm above the opening (since this region was where the differences between low- and high-friction simulations was most apparent).
- (ii) To obtain time-averaged continuum fields, a temporal average $(\hat{f}(x, y, z))$ was calculated over the entire 20 time steps. For each general field, f(x, y, z, t), this average was calculated using the trapezium numerical integration method applied to the following equation:

$$\hat{f}(x,y,z) = \frac{1}{t_f - t_0} \int_{t_0}^{t_f} f(x,y,z,t) dt.$$

(iii) To obtain depth-averaged continuum fields, a spatial average $(\hat{f}(x,z))$ was calculated over the entire silo depth. For each temporally averaged field, $\hat{f}(x,y,z)$, this average was calculated using the trapezium numerical integration method applied to the following equation:

$$\overline{\hat{f}(x,z)} = \frac{1}{D} \int_{0}^{D} \hat{f}(x,y,z,t) \, \mathrm{d}y.$$

- (iv) These temporally and depth-averaged continuum fields are then used to produce the 2D contour plots in the electronic supplementary data. Additionally, these 2D coarse-grained (spatially and temporally) averaged data are used to calculate the inertial number and solids fraction data at each point in the region R_1 , to be presented in figure 12.
- (v) To reduce noise and to quantitatively compare results from the low- and high-friction cases, and the results of changing L, a spatial average of the fields was calculated in a smaller region, $R_2 \subset R_1$, just above the silo opening. If (O_x, O_y) is the coordinate of the middle of one opening for any given silo, then the average was calculated over the region $R_2 = (O_x 7.25, O_x + 7.25) \, \text{mm} \times (O_y, O_y + 14) \, \text{mm}$, i.e. overhanging each opening on each side by $0.25 \, \text{mm}$ and from the opening to $14 \, \text{mm}$ above it. This average was calculated numerically using the trapezium rule applied to both the x and z (width and height) directions. The result was a single number which quantified the average value of a given scalar/vector field in the opening region. This 'opening average' was applied to each silo and used to produce figures $10 \, \text{and} \, 11$.

Figure 10 is a plot of the average 2D tensorial shear rate $(\dot{\gamma} = \sqrt{(\partial_x v_y + \partial_y v_x)^2 + (\partial_x v_x - \partial_y v_y)^2}$, where v_x, v_y are the horizontal and vertical coarse-grained velocity components, respectively) calculated just above each opening as a function of opening spacing L for the low- and high-friction cases. The spatial derivatives of the velocity components were numerically evaluated using the gradient function in Matlab. The solid and dashed horizontal lines correspond to the values of shear rate observed for the small single opening (i.e. a single opening of width $D_0 = 14 \, \text{mm}$), while the values on the line L = 0 (i.e ≈ 13 for the high- and ≈ 11.8 for the low-friction cases) refer to the case of a large single opening ($D_0 = 28 \, \text{mm}$). From this figure, three observations are made:

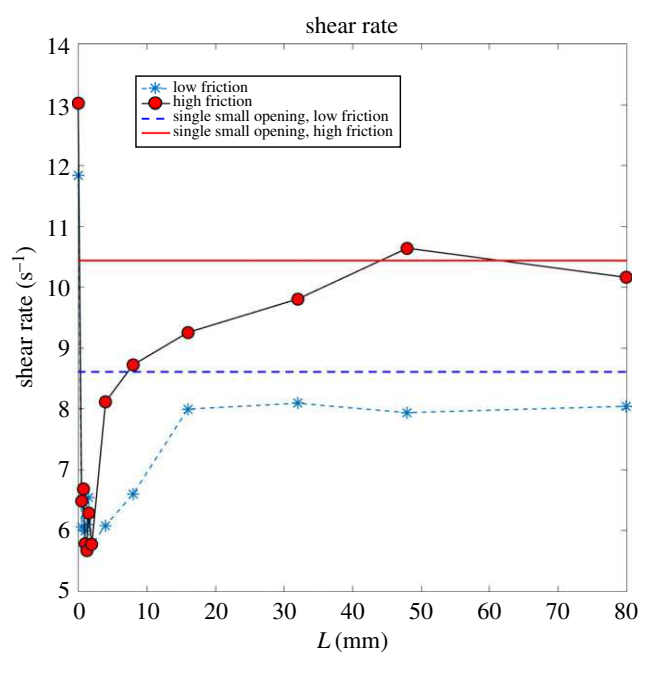


Figure 10. Shear rate observed just above an opening as a function of opening separation *L* from DEM numerical experiments. Error bars are smaller than the symbol size. (Online version in colour.)

- (1) As soon as L > 0, the value of the shear rate drops rapidly from the single large case (L = 0), and the value of shear rate for $0 < L \le 2$ mm is roughly constant for both the lowand high-friction experiments. This is consistent with the results for the flow rate, where the rate rapidly drops as L > 0 and oscillates between close values for $0 < L \le 2$ mm.
- (2) In the high-friction case, the shear rate rapidly rises at L = 4 mm, while in the low-friction case the increase is much more steady and less sharp.
- (3) As L increases past ≈ 16 mm, the shear rates for both cases approach the rate for a single opening (i.e. the two horizontal lines). However, the high-friction case gets much closer to this rate (the last two data points at 48 and 80 mm are less than 2.6% from the small single opening value) than the low-friction case (the last two data points at 48 and 80 mm are greater than 6.5% from the small single opening value). However, it is apparent that, between 16 and 80 mm, the shear rate for the low-friction case is largely constant. This is in contrast to the high-friction case, where the shear rate continues to rise to close to the expected equilibrium value.

To further study the behaviour of the system as L changes, and for low and high interparticle frictions, we derive other relevant parameters from our DEM simulations. Using the coarse-grained fields, we calculate the average solid pressure as one-third of the trace of the three-dimensional stress tensor $(P=1/3\mathrm{Tr}(\sigma))$. The granular inertial number is a dimensionless quantity that quantifies the importance of inertial to imposed forces, and is calculated as $I=d\dot{\gamma}\sqrt{\rho_p}/\sqrt{P}$. The solids fraction can be derived from the coarse-grained density as $\phi=\rho^{CG}/\rho_p$, while the apparent viscosity of the flow is calculated as $\eta=\tau/\dot{\gamma}$. Here, the deviatoric stress tensor invariant $\tau=\sqrt{1/2\tau_{ij}\tau_{ij}}$, where $\tau_{ij}=\sigma_{ij}-\delta_{ij}P$, where δ_{ij} is the Kronecker delta, and repeated indices imply summation. Figure 11 displays the results of calculating these properties for our DEM experiments. As for the shear rate figure, we note the following points about our results.

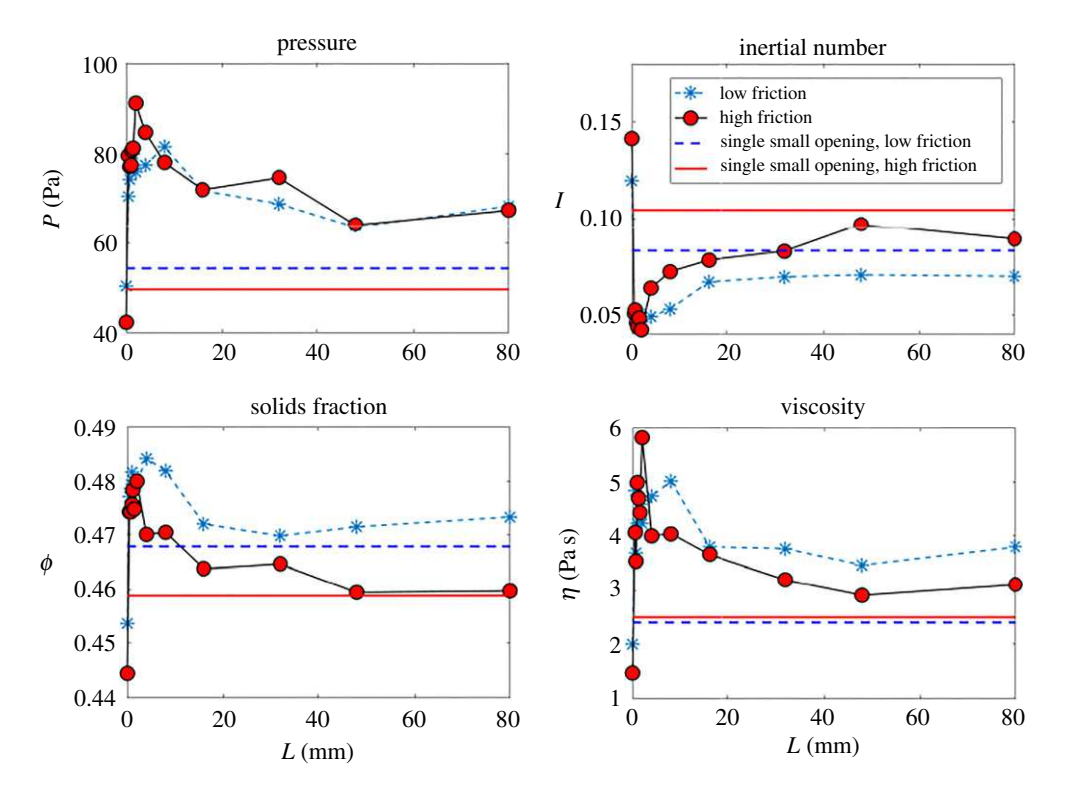


Figure 11. Pressure (*a*), inertial number (*b*), solids fraction (*c*) and apparent viscosity (*d*) observed just above an opening as a function of opening separation *L* from DEM numerical experiments. Error bars are smaller than the symbol size. (Online version in colour.)

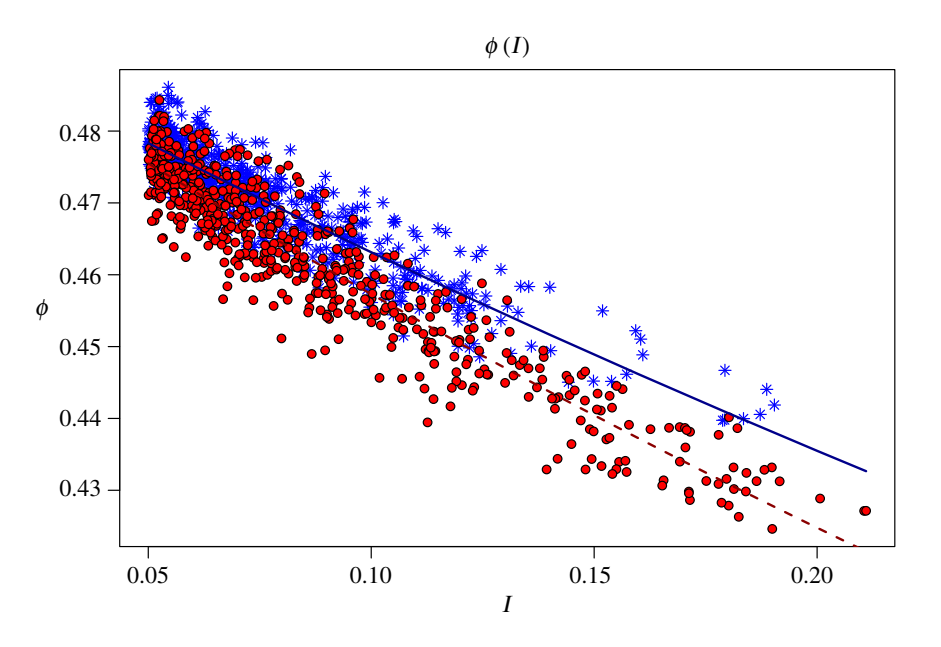


Figure 12. Statistical model fitting of solids fraction data for l > 0.05. The red circles are the high-friction data, while the blue markers are the low-friction data. There is a small amount of numerical error in the DEM simulation, but this is smaller than the symbol size. (Online version in colour.)

- (1) For $0 < L \le 2$ mm, we note a very large pressure spike for both the low- and high-friction cases of greater than 40% of the pressure value for the large single opening. The pressure is slightly more in the high-friction case, but still comparable. We note that for L < 2 mm the pressure is clustered, as was the shear rate and flow rate. In this regime, the inertial number falls to about a third of what it was for the single large opening, for both low and high friction. This suggests that the imposed forces (pressure) are of more importance in defining the flow structure than inertia/collisions. We again note the clustering of inertia number values in this range of L. The solids fraction is also at its maximum in this range of L. This suggests that, for $0 < L \le 2$ mm, the flow at the opening is at its most dense. We also note that the values are clustered, and similar for low or high friction. However, the differences in the actual values compared with the large single values are relatively small (less than 8% for the high friction, and 6% for low friction). It is unclear what effect this difference will have on the flow. The viscosity also displays clustering, but to a much lesser extent. For example, the value of viscosity at L = 2 mm is ≈ 1.6 times larger than at L = 0.5 mm. It is also apparent that at this range the viscosity is at a maximum.
- (2) For $4 \lesssim L \lesssim 32$ mm, we observe a steady decrease in the pressure, solids fraction, and viscosity for both low- and high-friction experiments. At L = 4 mm, as in the shear rate figure, the inertial number jumps rapidly for the high-friction case, but rises gradually for the low-friction case (which is expected, owing to the definition of I).
- (3) For $L \gtrsim 32 \,\mathrm{mm}$ we note that the pressure has not approached the hypothesized equilibrium value (i.e. the value of a small single opening). In fact, the value is $\approx 25\%$ greater in the low-friction case, and \approx 35% in the high-friction case. Contrast this with the shear rate at large L, where the rate is much closer to the equilibrium rate (less than 7%). It appears that, even at very wide spacings, the two openings still interact to increase the pressure above what is expected for two non-interacting openings. This could be a result of wall interaction, and should be further studied. Likewise, the inertial number at large L does not quite reach its non-interacting value (i.e. the value for a small single opening). However, the solids fraction in the high-friction case is very close to the small single opening value, while the low-friction solids fraction at large L is also relatively close. The largest difference between the two frictions at large L is in the viscosity. As L increases past $L \approx 32$ mm, the viscosity of the high-friction simulation decreases until it is $\approx 25\%$ larger than the small single opening value. However, in the range $16 < L < 80 \,\mathrm{mm}$, the value of the apparent viscosity for the low-friction simulation is quite consistent, being \approx 58% larger than the small single value. The value of viscosity at $L=80\,\mathrm{mm}$ is 22% larger in the low-friction case than in the high-friction case. While this initially seems counterintuitive, the observation that the shear rate for L > 16 mm is not increasing for the low-friction case, while it is for the high-friction one, fully explains this phenomenon. It is this observation that appears to explain the difference between the two flow rate behaviours: the monotonic and the flow rate minimum, rising to equilibrium. For both low- and high-friction granular materials, as L increases from 0 the shear rate rapidly drops, the pressure and viscosity rapidly increase, as does the flow rate. Both the highand low-friction cases reach a low in the flow rate at around $L/d \approx 8$ (which is ≈ 16 mm in our DEM experiment). As L increases past this value, for the high-friction case the shear rate continues to increase, hence the viscosity continues to drop, and the flow rate increases. However, for the low-friction case, the shear rate remains essentially constant, hence the viscosity remains essentially constant, and the flow rate slowly decreases. This result fully explains the discrepancy between previous DEM and experimental results, and the results from pedestrian dynamics [37,40].

Our results also indicate that the solids fraction difference between the low- and high-friction cases may not contribute significantly (compared with the effect of the shear rate behaviour as *L* is increased) to the dynamic behaviours observed. However, we note that changing the inter-particle friction value does in fact change the packing of the particles. It is also known that the solids

fraction is a decreasing function of the inertial number [51]. To test whether the solids fraction was significantly different between our high- and low-friction experiments we calculate the solids fraction and inertial number over the whole coarse-grained region ($R_1 = W \times D \times (0:5 \text{ cm})$) and plot this in figure 12. Owing to a significant amount of scatter in the data at low inertial numbers, in figure 12, we examine only the data where I > 0.05 and fit this to the $\phi(I)$ model of [52],

$$\phi(I) = \frac{a_1}{1 + a_2 I'} \tag{5.9}$$

where a_1 and a_2 are fitting parameters. It is shown in figure 12 that, for higher inter-particle friction, the solids fraction is lower at large I, indicating that flowing high-friction granular materials dilate more than low-friction ones. Using the standard nonlinear regression function found in the R statistical software application [53], we find

$$a_1 = 0.495$$
 and $a_2 = 0.678$

for the low-friction data and

$$a_1 = 0.495$$
 and $a_2 = 0.829$

for the high-friction data, with a statistically significant difference between the two sets of data for the a_2 parameter. Although this did not appear to be a significant effect for the DEM experiments (compared with the effect of the shear rate) that we performed, it could be that, for very low or very high values of inter-particle friction, the flow rate interaction behaviour is significantly altered by the dilation of the flow near the opening.

6. Discussion

In this work, we have combined imaging (PIV) and flow rate experiments with DEM to study the effect of opening separation distance in a rectangular silo with two symmetrically placed openings. In particular, we aimed to solve the discrepancy in the literature between DEM and experimental work in silos [37,38], where the flow rate decreased monotonically with opening separation distance, *L*, and pedestrian dynamics results [40], which had a local minimum flow rate behaviour.

We measured the mass flow rate of mustard seeds, amaranth and sand as a function of the opening separation distance. It was shown that in all cases we recovered a local minimum in the flow rate, as in the pedestrian dynamics study [40]. When the separation distance was normalized by the particle diameter the local minimum in the flow rate occurred at the same value: $L/d \approx 7.5$. We also observed a rapid decrease in the flow rate as L increased from 0 (a single large opening), and oscillatory behaviour in the flow rate for L/d < 4.

Our PIV analysis on mustard seeds in our silo gave a visual description of the interaction of two openings as the distance between them increased. Plots of velocity, velocity divergence, shear rate magnitude and a thresholded version of shear rate magnitude were presented. An interesting observation was that, for widely spaced openings, the shear rate in the bulk of the bin was much lower than in the single opening case. We believe that this could have implications for shear-induced size segregation of polydisperse granular materials during silo discharge.

We repeated our physical experimental results using DEM numerical experiments for a low and a high value of inter-particle friction. It was shown that the flow rate behaviour for the low-friction case was monotonic, as previously found in the literature [37,38], but a local minimum in the rate was observed for the high-friction case, as seen in our physical experiments, and in the pedestrian dynamics model [40]. Additionally, the local minimum was observed at approximately the same opening separation spacing, $L/d \approx 7.5$, as in our experiments. Furthermore, oscillatory behaviour in the flow rate for $L < 2 \, \text{mm}$ was observed for both the low- and high-friction cases; an observation not previously made in the literature (indeed, in previous work only one value of opening spacing L was below $2 \, \text{mm}$ [38]).

A coarse-graining routine was applied to the DEM results to generate continuum fields. It was shown that, in the small *L* oscillatory flow rate regime, the pressure, solids fraction and viscosity

were significantly larger than for single openings or large L, while the inertial number and shear rate were significantly smaller. As yet we are not able to fully explain the oscillatory behaviour. It was found that for $L \gtrapprox 16\,\mathrm{mm}$ the viscosity in the low-friction case was essentially constant as L continued to increase, while it continued to reduce for the high-friction case. This effect was due to the fact that, for $L \gtrapprox 16\,\mathrm{mm}$, the shear rate in the low-friction case was constant as L increases, while in the high-friction case the shear rate continued to increase.

We, therefore, conclude that the discrepancy in the literature between the flow rate behaviour of granular objects leaving a container with two exit openings (be it a silo or a room) is simply due to the value of inter-particle friction.

Data accessibility. Matlab data files for PIV velocity measurements, Excel sheets of mass flow rate data, an example MFIX DEM and Matlab course-graining code are all available as electronic supplementary material. Authors' contributions. L.A.F. and C.E.D. designed the silo experiments. L.A.F. and E.C.P.B. conducted all the experiments. E.C.P.B. ran the DEM simulations. L.A.F. wrote the coarse-graining code. M.F. and A.W. designed and built the load cell flow rate device. A.J.R.G. contributed to data analysis and statistical fitting. All authors contributed to conceptual development and refinement of the manuscript.

Competing interests. We declare we have no competing interests.

Funding. The research of L.A.F. was supported by the Royal Society of New Zealand, RFT-MAU1501-PD and MAU1712. Additional support was provided by the Royal Society of New Zealand Marsden Fund (contract no. 15-MAU-085) and the New Zealand Natural Hazards Research Platform (contract no. 2015-MAU-02-NHRP). E.C.P.B. was supported by National Science Foundation grant no. EAR 1650382 (J.D.).

Acknowledgements. The authors thank J. Edwards for the use of laboratory space.

References

- 1. Dohrn-van Rossum G. 1996 *History of the hour: clocks and modern temporal orders*. Chicago, IL: University of Chicago Press.
- 2. Garfinkel Y, Ben-Shlomo D, Kuperman T. 2009 Large-scale storage of grain surplus in the sixth millennium BC: the silos of Tel Tsaf. *Antiquity* 83, 309–325. (doi:10.1017/S0003598X00098458)
- 3. Andreotti B, Forterre Y, Pouliquen O. 2013 *Granular media: between fluid and solid*. Cambridge, UK: Cambridge University Press.
- 4. Jop P, Forterre Y, Pouliquen O. 2006 A constitutive law for dense granular flows. *Nature* **441**, 727–730. (doi:10.1038/nature04801)
- 5. MiDi G. 2004 On dense granular flows. Eur. Phys. J. E-Soft Matter 14, 341–365.
- Guillard F, Marks B, Einav I. 2017 Dynamic X-ray radiography reveals particle size and shape orientation fields during granular flow. Sci. Rep. 7, 8155. (doi:10.1038/s41598-017-08573-y)
- 7. Badetti M, Fall A, Roux JN. 2017 Rheology of wet granular materials under continuous shear: experiments and simulations. *EPJ Web Conf.* **140**, 08019. (doi:10.1051/epjconf/201714008019)
- 8. Fall A, Ovarlez G, Hautemayou D, Mézière C, Roux JN, Chevoir F. 2015 Dry granular flows: rheological measurements of the μ (I)-rheology. *J. Rheol.* **59**, 1065–1080. (doi:10.1122/1. 4922653)
- 9. Ristow G. 1996 Dynamics of granular materials in a rotating drum. *Europhys. Lett.* **34**, 263. (doi:10.1209/epl/i1996-00109-0)
- Yang H, Jiang G, Saw H, Davies C, Biggs MJ, Zivkovic V. 2016 Granular dynamics of cohesive powders in a rotating drum as revealed by speckle visibility spectroscopy and synchronous measurement of forces due to avalanching. *Chem. Eng. Sci.* 146, 1–9. (doi:10.1016/j. ces.2016.02.023)
- 11. Breard EC, Lube G, Jones JR, Dufek J, Cronin SJ, Valentine GA, Moebis A. 2016 Coupling of turbulent and non-turbulent flow regimes within pyroclastic density currents. *Nat. Geosci.* 9, 767–771. (doi:10.1038/ngeo2794)
- 12. Henann DL, Kamrin K. 2013 A predictive, size-dependent continuum model for dense granular flows. *Proc. Natl Acad. Sci. USA* 110, 6730–6735. (doi:10.1073/pnas.1219153110)
- 13. Gray J, Edwards A. 2014 A depth-averaged [mu](I)-rheology for shallow granular free-surface flows. *J. Fluid Mech.* **755**, 503. (doi:10.1017/jfm.2014.450)
- 14. Staron L, Phillips JC. 2016 How large grains increase bulk friction in bi-disperse granular chute flows. *Comput. Part. Mech.* **3**, 367–372. (doi:10.1007/s40571-015-0068-1)

- 15. Bouzid M, Trulsson M, Claudin P, Clément E, Andreotti B. 2013 Nonlocal rheology of granular flows across yield conditions. *Phys. Rev. Lett.* **111**, 238301. (doi:10.1103/PhysRev Lett.111.238301)
- 16. Fullard LA, Davies CE, Wake GC. 2013 Modelling powder mixing in mass flow discharge: a kinematic approach. *Adv. Powder Technol.* 24, 499–506. (doi:10.1016/j.apt.2013.02.005)
- 17. Staron L, Lagrée PY, Popinet S. 2014 Continuum simulation of the discharge of the granular silo. *Eur. Phys. J. E* 37, 5. (doi:10.1140/epje/i2014-14005-6)
- 18. Fullard L, Davies C, Lube G, Neather A, Breard E, Shepherd B. 2017 The transient dynamics of dilation waves in granular phase transitions during silo discharge. *Granular Matter* **19**, 6. (doi:10.1007/s10035-016-0685-2)
- 19. Staron L, Lagrée PY, Popinet S. 2012 The granular silo as a continuum plastic flow: the hourglass vs the clepsydra. *Phys. Fluids* **24**, 103301. (doi:10.1063/1.4757390)
- 20. Janda A, Harich R, Zuriguel I, Maza D, Cixous P, Garcimartín A. 2009 Flow-rate fluctuations in the outpouring of grains from a two-dimensional silo. *Phys. Rev. E* **79**, 031302. (doi:10.1103/PhysRevE.79.031302)
- 21. Sielamowicz I, Blonski S, Kowalewski T. 2005 Optical technique DPIV in measurements of granular material flows, part 1 of 3—plane hoppers. *Chem. Eng. Sci.* **60**, 589–598. (doi:10.1016/j. ces.2004.07.135)
- 22. Weinhart T, Labra C, Luding S, Ooi JY. 2016 Influence of coarse-graining parameters on the analysis of DEM simulations of silo flow. *Powder Technol.* **293**, 138–148. (doi:10.1016/j. powtec.2015.11.052)
- 23. Rubio-Largo SM, Janda A, Maza D, Zuriguel I, Hidalgo R. 2015 Disentangling the free-fall arch paradox in silo discharge. *Phys. Rev. Lett.* **114**, 238002. (doi:10.1103/PhysRevLett.114.238002)
- 24. Maza D, Janda A, Rubio-Largo SM, Zuriguel I, Hidalgo R. 2013 Velocity and density scaling at the outlet of a silo and its role in the expression of the mass flow rate. *AIP Conf. Proc.* **1542**, 674–677. (doi:10.1063/1.4812021)
- 25. Choi J, Kudrolli A, Bazant MZ. 2005 Velocity profile of granular flows inside silos and hoppers. *J. Phys. Condens. Matter* **17**, S2533. (doi:10.1088/0953-8984/17/24/011)
- 26. Sielamowicz I, Kowalewski TA, Błoński S. 2004 Central and eccentric granular material flows in bins/hoppers registered by DPIV optical technique. *Acta Agrophys.* **4**, 519–531.
- 27. Maiti R, Meena S, Das PK, Das G. 2016 Flow field during eccentric discharge from quasi-two-dimensional silos—extension of the kinematic model with validation. *AlChE J.* **62**, 1439–1453. (doi:10.1002/aic.v62.5)
- 28. Zhou Y, Lagrée PY, Popinet S, Ruyer P, Aussillous P. 2017 Experiments on, and discrete and continuum simulations of, the discharge of granular media from silos with a lateral orifice. *J. Fluid Mech.* **829**, 459–485. (doi:10.1017/jfm.2017.543)
- 29. Wilson T, Pfeifer C, Meysingier N, Durian D. 2014 Granular discharge rate for submerged hoppers. *Papers Phys.* **6**, 060010. (doi:10.4279/pip.060010)
- 30. Koivisto J, Korhonen M, Alava M, Ortiz CP, Durian DJ, Puisto A. 2017 Friction controls even submerged granular flows. *Soft Matter* **13**, 7657–7664. (doi:10.1039/c7sm00806f)
- 31. Cleary PW. 1999 The effect of particle shape on hopper discharge. In *Proc. 2nd Int. Conf. on CFD in the Minerals and Process Industries, Melbourne, Australia, 6–8 December 1999*, pp. 71–76. Clayton, Australia: CSIRO Publishing.
- 32. Börzsönyi T, Somfai E, Szabó B, Wegner S, Mier P, Rose G, Stannarius R. 2016 Packing, alignment and flow of shape-anisotropic grains in a 3D silo experiment. *New J. Phys.* 18, 093017. (doi:10.1088/1367-2630/18/9/093017)
- 33. Mondal S, Sharma MM. 2014 Role of flying buttresses in the jamming of granular matter through multiple rectangular outlets. *Granular Matter* **16**, 125–132. (doi:10.1007/s10035-013-0461-5)
- 34. Kunte A, Doshi P, Orpe AV. 2014 Spontaneous jamming and unjamming in a hopper with multiple exit orifices. *Phys. Rev. E* **90**, 020201. (doi:10.1103/PhysRevE.90.020201)
- 35. Kamath S, Kunte A, Doshi P, Orpe AV. 2014 Flow of granular matter in a silo with multiple exit orifices: jamming to mixing. *Phys. Rev. E* **90**, 062206. (doi:10.1103/PhysRevE.90.062206)
- 36. Maiti R, Das G, Das PK. 2017 Granular drainage from a quasi-2D rectangular silo through two orifices symmetrically and asymmetrically placed at the bottom. *Phys. Fluids* **29**, 103303. (doi:10.1063/1.4996262)
- (doi:10.1063/1.4996262)
 37. Zhang X, Zhang S, Yang G, Lin P, Tian Y, Wan JF, Yang L. 2016 Investigation of flow rate in a quasi-2D hopper with two symmetric outlets. *Phys. Lett. A* 380, 1301–1305. (doi:10.1016/j.physleta.2016.01.046)

- 38. Xu C, Wang FL, Wang LP, Qi XS, Shi QF, Li LS, Zheng N. 2018 Inter-orifice distance dependence of flow rate in a quasi-two-dimensional hopper with dual outlets. *Powder Technol.* **328**, 7–12.
- 39. Davies CE, et al. 1997 Discharge of granular materials through adjacent orifices and multiorifice plates. In *Proc. IPENZ Annu. Conf. 1997, Engineering our Nation's Future; Volume 2, Wellington, New Zealand, 7–10 February 1997*, p. 62. Wellington, New Zealand: Institution of Professional Engineers New Zealand.
- 40. Sticco IM, Frank GA, Cerrotta S, Dorso CO. 2017 Room evacuation through two contiguous exits. *Physica A* **474**, 172–185. (doi:10.1016/j.physa.2017.01.079)
- 41. Garcimartín A, Pastor J, Ferrer L, Ramos J, Martín-Gómez C, Zuriguel I. 2015 Flow and clogging of a sheep herd passing through a bottleneck. *Phys. Rev. E* **91**, 022808. (doi:10.1103/PhysRevE.91.022808)
- 42. Thielicke W, Stamhuis EJ. 2014 PIVlab—towards user-friendly, affordable and accurate digital particle image velocimetry in MATLAB. *J. Open Res. Softw.* **2**, e30. (doi:10.5334/jors.bl)
- 43. Thielicke W. 2014 The flapping flight of birds–analysis and application. PhD thesis Rijksuniversiteit Groningen, Groningen, The Netherlands.
- 44. Beverloo WA, Leniger HA, Van de Velde J. 1961 The flow of granular solids through orifices. *Chem. Eng. Sci.* **15**, 260–269. (doi:10.1016/0009-2509(61)85030-6)
- 45. Pastor JM *et al.* 2015 Experimental proof of faster-is-slower in systems of frictional particles flowing through constrictions. *Phys. Rev. E* **92**, 062817. (doi:10.1103/PhysRevE.92.062817)
- 46. Gella D, Maza D, Zuriguel I, Ashour A, Arevalo R, Stannarius R. 2017 Linking bottleneck clogging with flow kinematics in granular materials: the role of silo width. *Phys. Rev. Fluids* **2**, 084304. (doi:10.1103/PhysRevFluids.2.084304)
- 47. Garg R, Galvin J, Li T, Pannala S. 2012 Open-source MFIX-DEM software for gas–solids flows: part I—verification studies. *Powder Technol.* **220**, 122–137. (doi:10.1016/j.powtec.2011.09.019)
- 48. Li T, Garg R, Galvin J, Pannala S. 2012 Open-source MFIX-DEM software for gas-solids flows: part II—validation studies. *Powder Technol.* **220**, 138–150. (doi:10.1016/j.powtec.2011.09.020)
- 49. Li J, Webb C, Pandiella S, Campbell GM. 2002 A numerical simulation of separation of crop seeds by screening—effect of particle bed depth. *Food Bioprod. Process.* **80**, 109–117. (doi:10.1205/09603080252938744)
- 50. Rubio-Largo S, Maza D, Hidalgo R. 2017 Large-scale numerical simulations of polydisperse particle flow in a silo. *Comput. Part. Mech.* **4**, 419–427. (doi:10.1007/s40571-016-0133-4)
- 51. Forterre Y, Pouliquen O. 2008 Flows of dense granular media. *Annu. Rev. Fluid Mech.* 40, 1–24. (doi:10.1146/annurev.fluid.40.111406.102142)
- 52. Amarsid L, Delenne JY, Mutabaruka P, Monerie Y, Perales F, Radjai F. 2017 Viscoinertial regime of immersed granular flows. *Phys. Rev. E* **96**, 012901. (doi:10.1103/Phys RevE.96.012901)
- 53. R Foundation. 2018 *R: A language and environment for statistical computing*. Vienna, Austria: R Foundation for Statistical Computing.